

Ag/Ag₂O with NIR-Triggered Antibacterial Activities: Photocatalytic Sterilization Enhanced by Low-Temperature Photothermal Effect

Ruojing Qian^{1,3,*}, Zhaoyu Xu^{4,*}, Xingyu Hu¹⁻³, Suru Liu¹⁻³, Yao Mai¹⁻³, Xinzhi Tan¹⁻³, Xiaofan Su¹⁻³, Mingyan Jiang¹⁻³, Wei Tang¹⁻³, Weidong Tian¹⁻³, Li Xie¹⁻³

¹State Key Laboratory of Oral Diseases & National Clinical Research Center for Oral Diseases & National Engineering Laboratory for Oral Regenerative Medicine, West China Hospital of Stomatology, Sichuan University, Chengdu, People's Republic of China; ²Engineering Research Center of Oral Translational Medicine, Ministry of Education, West China Hospital of Stomatology, Sichuan University, Chengdu, People's Republic of China; ³Department of Oral and Maxillofacial Surgery, West China Hospital of Stomatology, Sichuan University, Chengdu, People's Republic of China; ⁴Department of Oral Implantology, West China Hospital of Stomatology, Sichuan University, Chengdu, People's Republic of China

*These authors contributed equally to this work

Correspondence: Weidong Tian; Li Xie, State Key Laboratory of Oral Diseases & National Clinical Research Center for Oral Diseases & Engineering Research Center of Oral Translational Medicine, Ministry of Education & National Engineering Laboratory for Oral Regenerative Medicine, West China Hospital of Stomatology, Sichuan University, Chengdu, Sichuan, 610041, People's Republic of China, Tel +86-28-85502156; +86-28-85503499, Email drtwd@sina.com; samuel@163.com

Purpose: A synergistic antibacterial system employing photocatalytic performance and low-temperature photothermal effect (LT-PTT) with the potential for infectious skin wound healing promotion was developed.

Methods: Ag/Ag₂O was synthesized with a two-step method, and its physicochemical properties were characterized. After its photocatalytic performance and photothermal effect were evaluated under 0.5 W/cm² 808 nm NIR laser irradiation, its antibacterial activities in both planktonic and biofilm forms were then studied in vitro targeting *Staphylococcus Aureus* (*S. aureus*), and the biocompatibility was tested with L-929 cell lines afterward. Finally, the animal model of dorsal skin wound infection was established on Sprague-Dawley rats and was used to assess infectious wound healing promotion of Ag/Ag₂O in vivo.

Results: Ag/Ag₂O showed boosted photocatalytic performance and local temperature accumulation compared with Ag₂O when exposed to 0.5 W/cm² 808 nm NIR irradiation, which therefore endowed Ag/Ag₂O with the ability to kill pathogens rapidly and cleavage bacterial biofilm in vitro. Furthermore, after treatment with Ag/Ag₂O and 0.5 W/cm² 808 nm NIR irradiation, infectious wounds of rats realized skin tissue regeneration from a histochemical level.

Conclusion: By exhibiting excellent NIR-triggered photocatalytic sterilization ability enhanced by low-temperature photothermal effect, Ag/Ag₂O was promising to be a novel, photo-responsive antibacterial agent.

Keywords: semiconductor/metal hybrid, antibacterial agent, photo-responsive antibacterial activity, reactive oxygen species, infectious wound skin model

Introduction

Bacterial infection has been consistently affecting public health and the problem.^{1,2} However, resulting from the long-term misuse and overuse of antibiotics, the emergence of antibiotic-resistant bacteria has become an even trickier issue, which therefore evoked the need for effective antibacterial therapeutic strategies without the side effects of causing bacterial resistance.³⁻⁶ Recent studies aiming to tackle these problems have attached much attention to developing photo-responsive materials due to their robust and rapid bactericidal activities.⁷⁻⁹ In phototherapeutic approaches, photo-responsive materials, in the first place, respond to light at appropriate wavelengths, ranging from ultraviolet (UV) to NIR, which is then followed by the production of reactive oxygen species (ROS) and hyperthermia.⁷ In comparison with conventional treatment, photo-responsive inactivation of pathogens is much faster, leaving bacteria no space to evolve

into those with defense mechanisms. When considering practical biomedical applications, NIR outcompetes other light sources with deeper penetration and less damage to normal tissues nearby.^{10,11} However, many prevalently applied photo-activated materials could only respond to visible light or even UV due to their inherent electrical properties, which thus prioritize the employment of NIR-responsive materials.

Among various kinds of photo-responsive materials, semiconductors have attracted much interest,^{12–15} among which silver oxide (Ag_2O), a p-type semiconductor-based photocatalyst with an intrinsic narrow band gap of 1.3 eV, could be theoretically activated by NIR up to ~ 954 nm ($\lambda = 1240/E_g$),^{16,17} and thus has the potential of excellent responsibility to 808 nm NIR. Present studies of its photo-responsibility mainly focused on its photocatalytic activities in environmental pollution remediation.^{18–20} Jiang et al, for instance, designed superhydrophobic Ag_2O with excellent photocatalytic degradation performance of floating oils.²¹ However, the photocatalytic antibacterial performance of Ag_2O has rarely been reported, although some studies mentioned that Ag_2O nanoparticles exhibited antibacterial ability due to their morphology or the release of silver ions (Ag^+).^{16,22–24} Additionally, in some previous studies, it was reported that the formation of $\text{Ag}/\text{Ag}_2\text{O}$ heterostructures enhanced the photocatalytic ability of Ag_2O when triggered by visible light.^{25,26} With the deposition of silver (Ag) on the surface of Ag_2O , on the one hand, there would be an energy difference between the valence band of the semiconductor and the Fermi energy of the metal, named as Schottky barrier, capturing electrons, and therefore preventing them from recombining with holes, which in turn helps increase the photocatalytic activity.^{27,28} On the other hand, the surface electrons of silver nanoparticles (AgNPs) could oscillate when triggered by NIR light, a phenomenon known as the localized surface plasmon resonance (LSPR), and such oscillation could lead to the local temperature increase, which could further be utilized for the photon-heat energy conversion as well as a propellant for photocatalytic performance.^{29,30} In addition, silver nanoparticles (AgNPs) have exhibited broad-spectrum and effective antimicrobial activity in previous studies and thus have been prevalently applied as promising antibacterial agents.^{31,32} Besides, there were also various AgNP -containing medical supplies already in use on the market, such as wound dressings (ACTICOAT*HMP Global, Inc.) and hemostatic gelatine sponge (ROEKO Gelatamp, COLTENE), which therefore verified the high possibility of the safe application of AgNPs . There was no conclusion about their cytotoxicity yet, while some reviews mentioned that AgNPs could exhibit anti-inflammatory properties to some extent and were biocompatible with fibroblasts.³³ Accordingly, a new synergistic antibacterial system was fabricated on the basis of $\text{Ag}/\text{Ag}_2\text{O}$ heterostructures, in which the excellent photocatalytic performance and the LT-PTT effect complemented each other, achieving robust antibacterial activity in vitro and in vivo, and promoting the infectious skin wound healing within 8 days in the animal models when irradiated by low power intensity 808 nm NIR irradiation.

Herein, in our work, we fabricated $\text{Ag}/\text{Ag}_2\text{O}$ heterojunctions through a facile and classical sodium borohydride reduction method, leaving the reduced silver (Ag^0) deposited on the surface of Ag_2O (Figure 1).³⁴ The physical and chemical properties of the as-synthesized hybrid material were examined with various characterization methods, followed by a series of evaluations in terms of its photocatalytic performance enhanced by the photothermal effect of 808 nm NIR laser irradiation. Afterward, the biocompatibility of $\text{Ag}/\text{Ag}_2\text{O}$ was evaluated by co-incubation of mouse fibroblasts (L-929 cell lines). Finally, its boosted antibacterial activity in vitro and in vivo under the same irradiation conditions was analyzed. We supposed that the promising outcome of NIR-triggered antibacterial activities of $\text{Ag}/\text{Ag}_2\text{O}$ could shed light on the ongoing exploration for antibiotics-free antimicrobial strategies.

Materials and Methods

Chemicals and Materials

All chemicals were purchased from Aladdin (Aladdin Biochemical Technology Co., Ltd, Shanghai, China) unless otherwise noted. The infrared diode laser was obtained from Changchun New Industries Optoelectronics Tech. Co., Ltd.

Preparation of $\text{Ag}/\text{Ag}_2\text{O}$ Heterostructures

Firstly, Ag_2O was prepared by an ion-exchange method based on previous research with modification. In short, 0.3 M NaOH , 0.2 M AgNO_3 , and 0.1 M H_3BO_3 were thoroughly mixed in 50 mL deionized water under magnetic stirring

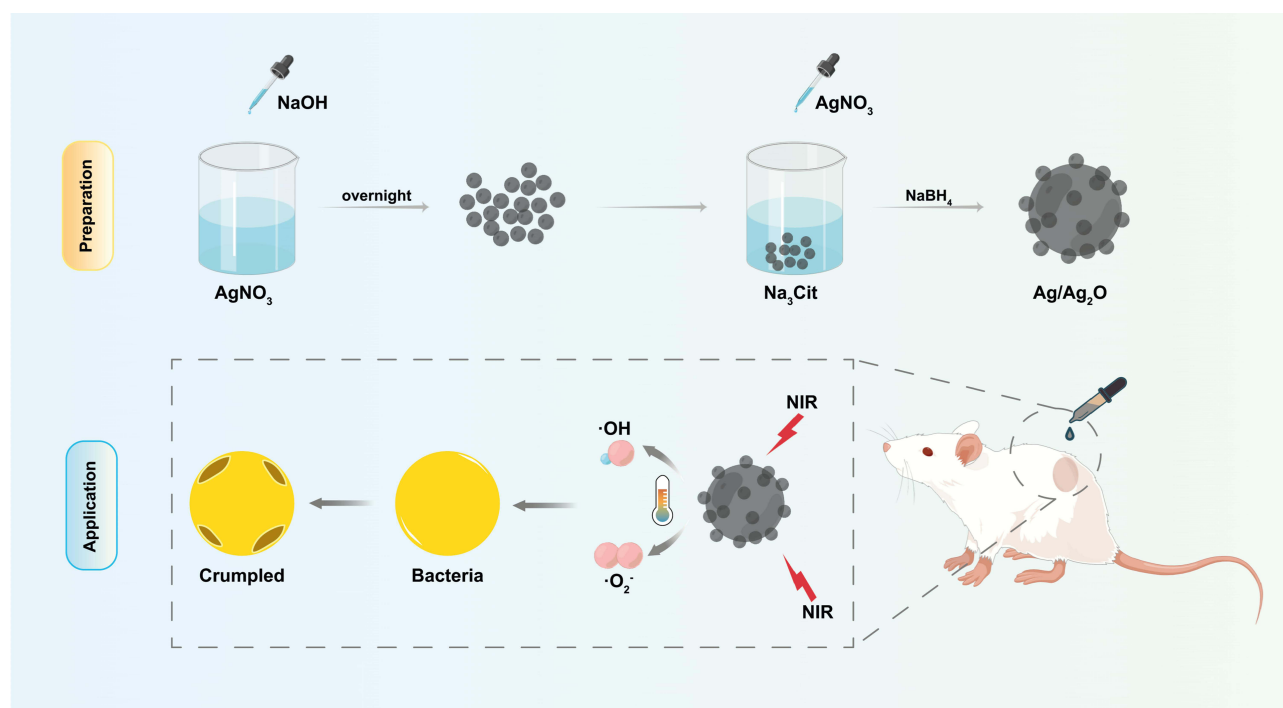


Figure 1 Schematic illustration of the synthetic route of Ag/Ag₂O and its NIR-triggered photo-responsive antibacterial activities.

overnight to ensure a complete reaction. Next, 200 mg of the as-synthesized Ag₂O particles were dispersed in 40 mL 2.5×10^{-4} M sodium citrate solution and 20 mL 2.5×10^{-4} M AgNO₃ solution for 3 h. Then, 0.6 mL 0.1 M ice-cooled NaBH₄ was pipetted dropwise into the solution. Afterward, the final product was washed and dried in a vacuum at room temperature overnight.

Characterization

The surface morphology images were captured by scanning electron microscopy (SEM, Thermo Fisher Apreo 2C). The microstructure images were obtained with transmission electron microscopy (TEM, FEI F200S) and high-resolution TEM. X-ray diffraction (XRD) patterns were recorded using Cu-K α irradiation ranging from 20° to 80° (Bruker D8 Advance) to determine the composition of the as-prepared samples. X-ray photoelectron spectra (XPS) were acquired with a non-monochromatized Al-K α X-ray source on a Thermo Fisher ESCALAB 250Xi spectrometer. UV-vis-NIR diffuse absorbance spectra of the samples were recorded in the spectral region of 200–1000 nm with a Shimadzu UV-3600 Plus spectrophotometer.

Photothermal Effect Assessment

Firstly, the photothermal effect of 1 mg/mL Ag/Ag₂O was tested under 808 nm NIR (MDL-808, New Industries Optoelectronics Technology, Changchun, China) irradiation of different power intensity (0.25, 0.75, and 1 W/cm²). The changes in solution temperature during the process were monitored by a submerged thermocouple microprobe (TES-1310, TES Electrical Electronic Corporation) and recorded every 1 min, via which the appropriate irradiation power intensity of 808 nm NIR laser was determined for later experiments. Afterward, 1 mg/mL Ag₂O and Ag/Ag₂O were irradiated by an 808 nm NIR laser at the determined power density (0.5 W/cm²) for 10 min to evaluate the photothermal effect under such conditions. Likewise, the temperature shift was also recorded in the way mentioned above.

Photocatalytic Activity Evaluation

The recombination of photogenerated electron/hole pairs was evaluated by photoluminescence spectra (PL) via a fluorescence spectrophotometer (Hitachi F-4100). Then, the production of ROS (·OH, ·O₂⁻) after being irradiated

under 808 nm NIR laser (0.5 W/cm^2) for 10 min was evaluated via electron spin resonance (ESR) spectrometer (Bruker EMX-Plus) with 5,5-dimethyl-1-pyrroline N-oxide (DMPO) being the spin trap agent. Finally, the photocatalytic activities of each group were further assessed utilizing an organic dye (methylene blue, MB) degradation model. Specifically, 1 mg/mL of each sample was added into 20 ppm MB solution with or without NIR irradiation (808 nm, 0.5 W/cm^2) for 90 min. Subsequently, 200 μL of the suspension was collected every 10 min. Then it was centrifuged, the supernatant of which was added into a 96-well plate to measure the optical density (OD) values of MB at 664 nm with a spectrometer (Multiskan Go, Thermo, USA) to determine the concentration of MB. Similar experiments on the degradation of MB of Ag/Ag₂O+NIR were also carried out in an ice bath. To test the storage stability of the as-synthesized Ag/Ag₂O, the samples were first stored at room temperature without special protection from light. Then, the photocatalytic activity of newly fabricated Ag/Ag₂O (Fresh) and stored Ag/Ag₂O (Old) was compared. Also, the activity stability of Ag/Ag₂O was evaluated for 4 runs. After the first photocatalytic degradation process was done, the solution was centrifuged (10,000 r/min, 10 min) and washed three times to separate Ag/Ag₂O, which was then used in later repeated experiments.

Antibacterial Activities on Planktonic Bacteria

Staphylococcus aureus (*S. aureus*) was employed to evaluate the antibacterial activities by the plate counting method. To reach the logarithmic growth period, *S. aureus* was cultured in BHI broth at 37°C overnight. Next, experiments were conducted with different samples with or without NIR irradiation (808 nm, 0.5 W/cm^2). In brief, different materials of 1 mg/mL were separately added into the 10 mL bacterial suspension and underwent various treatments for 10 min, after which the suspension was diluted 10^5 times and dispersed onto BSA agar plates. Then, bacterial colonies were counted after incubation at 37°C for 24 h. The bactericidal efficiency of each group was calculated as the equation: Antibacterial Rate (%) = $\frac{A_0 - A}{A_0} \times 100\%$, where A_0 and A were the number of bacterial colonies before and after treatment, respectively.

Antibacterial Activities on Bacterial Biofilms

Glass slices were separately placed in a 24-well plate, on which *S. aureus* was seeded with 1% sucrose-containing BHI broth for 2 d to develop biofilms, during which the medium was changed every other day. On the third day, the medium was removed, and different materials of 1 mg/mL were added separately into the wells, followed by different treatments mentioned above. After treatment, the glass slices were rinsed with 0.9% saline three times. Live and dead bacteria were stained with Live/Dead bacterial viability fluorochrome according to the manufacturer's instruction and observed with confocal laser scanning microscopy (OLYMPUS FV1200, Japan). The resulting fluorescence intensity was measured by ImageJ, based on which the antibacterial ability of biofilms was calculated.

Biocompatibility Assessment

Mouse fibroblast cells (L-929 cells) were purchased from the American Type Culture Collection (USA) and were selected as the model cell to evaluate cell proliferation, survival, and migration in vitro in the presence of Ag/Ag₂O by CCK-8 assay and cell migration assay. L-929 cells were cultured with Dulbecco's modified eagle medium (DMEM) containing 14% FBS and 1% Penicillin-Streptomycin at 37°C. For the CCK-8 assay, L-929 cells were firstly inoculated into a 96-well plate at a density of 3×10^4 cells per well for 24 h. Then the medium was replaced by that mixed with different concentrations of Ag/Ag₂O (0, 10, 20, 50, 100 $\mu\text{g/mL}$). The cell proliferation after 24-hour incubation was detected by CCK-8 according to the manufacturer's instructions, and the OD value at 450 nm was recorded with a spectrophotometer. As for cell migration assay, L-929 cells were seeded into the upper chambers of a 24-well transwell plate (Corning, USA) at a density of 10^4 cells per well, and DMEM containing different concentrations of sterilized Ag/Ag₂O (0, 10, 20, 50, 100 $\mu\text{g/mL}$) were added into the lower chambers. After 24 h, the migrated cells were fixed with 4% paraformaldehyde, stained with 0.1% crystal violet, and imaged with a stereo microscope (SZX16, OLYMPUS). The total amount of migrated cells was counted via ImageJ and analyzed.

Infectious Skin Wound Healing Promotion in vivo

All animal experiments were performed according to protocols approved by the Institutional Animal Care and Use Committee (IACUC) at Sichuan University. Antibacterial activities in vivo were studied on infectious skin wound animal models (approved by West China Hospital of Stomatology Ethics Committee, Sichuan University, NO. WCHSIRB-D-2022-395). Male Sprague-Dawley (SD) rats (6–8 w, 100–120 g) were adapted, on which infectious skin wound was built by removing the dorsal skin of rats in the diameter of 7 mm, followed by spraying 100 μ L *S. aureus* ($\sim 1.5 \times 10^8$ CFU/mL) suspension onto it and covered with a pad film dressing (3M™ Tegaderm™) for 24 h. Subsequently, the rats were divided into four groups randomly: control, NIR, Ag/Ag₂O, and Ag/Ag₂O+NIR (n>3). In the Control group, the mice received no special treatment, while in the NIR group, the mice were treated with 0.5 W/cm² 808 nm NIR irradiation for 10 min. In the Ag/Ag₂O group, 1 mL Ag/Ag₂O suspension of 1 mg/mL was added dropwise to the infectious wound area. Moreover, in the Ag/Ag₂O+NIR group, the mice were treated with Ag/Ag₂O suspension of the same volume and concentration under the same NIR irradiation condition mentioned above. The wounds were photographed every 2 d, and the areas were measured with ImageJ. The healing ratio (HR) was calculated as the equation: $HR (\%) = \frac{A_0 - A}{A_0} \times 100\%$, in which A_0 represented the area of the initial wound, and A represented the wound area at the selected time point. On day 8, the rats were sacrificed, and the dorsal skin tissues were retrieved. The sample slices were later used for hematoxylin/eosin (H&E) staining and Masson trichrome staining, followed by observation with an optical microscope for histological analysis. From the H&E-stained slides, inflammatory cells were counted in five randomly selected fields (100x) according to previous studies.³⁵

Statistical Analysis

All numerical data were statistically analyzed with GraphPad Prism (Version 9.0.0, GraphPad Software, San Diego, CA, USA). The data were reported as the mean \pm standard deviation (SD), and the results were contrasted via ANOVA. A value of $P < 0.05$ was considered statistically significant. Statistical significance: * $p < 0.05$, ** $p < 0.01$, *** $p < 0.001$, **** $p < 0.0001$.

Results and Discussion

Sample Synthesis and Characterization

Ag/Ag₂O was successfully synthesized in a facile and easily accessible way. In some other studies, Ag/Ag₂O was either fabricated by the partial decomposition of Ag₂O under high temperature or by photoreduction using a high-powered xenon lamp,^{36,37} which made the process hard to manipulate. However, in this study, Ag/Ag₂O was synthesized in the way of facile reaction conditions, accessible reagents, and controllability, for which the formation of the heterostructures might be capable of being modulated by the researcher's ideas. SEM images of commercial Ag₂O and synthesized Ag/Ag₂O particles are exhibited in Figure 2a and b to show the particle morphology. The TEM and HRTEM images of Ag₂O (Figure 2c, d) implied that the particles were uniform and highly crystalline, with a lattice fringe at 0.270 nm, which could be attributed to the (111) plane of Ag₂O. Additionally, TEM and HRTEM images of Ag/Ag₂O (Figure 2e and f) indicated that the lattice fringes at 0.204 nm and 0.270 nm corresponded well to the (200) plane of metallic Ag and (111) plane of Ag₂O, respectively. XPS was employed to analyze the chemical state and surface elemental composition of Ag₂O and Ag/Ag₂O, and the results are shown in Figure 2g-j. The entire XPS spectrum of Ag₂O and Ag/Ag₂O is observed in Figure 2g and h, respectively, in which the peaks of C, O, and Ag were found. XPS spectra confirmed that the samples were primarily composed of silver (Ag) and oxygen (O), and the characteristic peak of O 1s was separated. The O 1s XPS spectrum (Figure 2i and j) has seen a slight increase in metal oxides content of Ag/Ag₂O (13.79 at%) in comparison with Ag₂O (12.28 at%). XRD patterns of the Ag₂O and Ag/Ag₂O (Figure 2k) displayed a series of diffraction peaks, which could be generally assigned to the cubic phase of Ag₂O (JCPDS card No.43–0997). Besides, the peaks at 38.116°, 44.277°, and 64.426° of Ag/Ag₂O samples were attributed to metallic Ag according to JCPDS file No.04–0783.^{38,39} A possible reason that the diffraction peak of Ag⁰ was also found in the samples of Ag₂O could also be attributed to its intrinsic unstableness. These results implied the coexistence of Ag and Ag₂O in the synthesized samples and suggested the possible formation of the heterojunction structures, laying a solid foundation for the future boost of photo-responsive performance. UV-Vis-NIR spectra (Figure 2l) demonstrated that both Ag₂O and Ag/Ag₂O had the

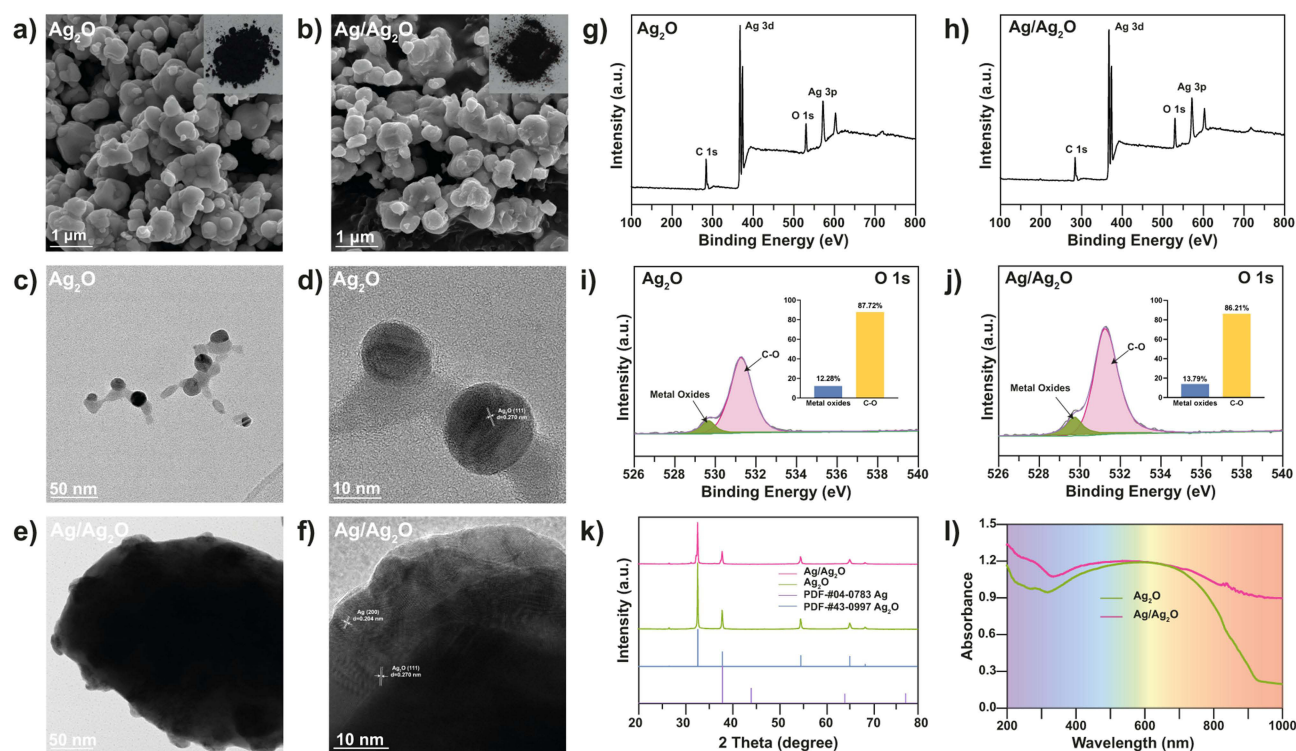


Figure 2 Characterization of Ag/Ag₂O heterostructures. SEM images of Ag₂O (a) and Ag/Ag₂O (b). The insets are the digital photographs of Ag₂O and Ag/Ag₂O, respectively. TEM (c) and HRTEM (d) images of Ag₂O. TEM (e) and HRTEM (f) images of Ag/Ag₂O. XPS survey spectra of Ag₂O (g) and Ag/Ag₂O (h). O 1s XPS spectra of Ag₂O (i) and Ag/Ag₂O (j). (The insets show the chemical composition of O 1s of the spectrum.) (k) X-ray diffraction patterns of Ag₂O and Ag/Ag₂O. (l) UV-Vis-NIR absorbance spectrum of Ag₂O and Ag/Ag₂O.

ability of broad-spectrum light response, ranging from ultraviolet to near-infrared (200–1000 nm), while Ag/Ag₂O exhibited more substantial absorbance of NIR light, implying subsequent better NIR-responsive performance of Ag/Ag₂O.

Photothermal Effect and Photocatalytic Performance

With many previous studies focusing on the photocatalytic performance of Ag₂O,^{16,17,40,41} the photothermal effect of it and Ag/Ag₂O under 808 nm NIR laser irradiation was studied for the first time to our knowledge. Firstly, the photothermal effect of Ag/Ag₂O under 808 nm NIR laser irradiation at different power intensities was evaluated (Figure 3a), from which we could tell that the local temperature of 1 mg/mL Ag/Ag₂O suspension increased to a different extent when illuminated by 808 nm laser at a power density of 0.25, 0.5, and 1 W/cm², and the power intensity of 1 W/cm² exhibited the most improvement in temperature within 10 min, the figure of which climbed up to 52.8°C. However, as local hyperthermia (>50°C) was generally known to have the potential to cause apoptosis of nearby normal tissue,⁴² we chose 0.5 W/cm² as the irradiation power density of later experiments. As shown in Figure 3b, the 0.5 W/cm² 808 nm laser could hardly heat the water, while for the Ag₂O-containing solution, the temperature accelerated to 33.5°C. By contrast, with the existence of Ag/Ag₂O, the temperature of the solution climbed up to 44°C under the same irradiation conditions, demonstrating that Ag/Ag₂O was more efficient in transforming the laser energy into heat, probably owing to the LSPR effect of the loaded Ag.^{28,30,43–45}

Photoluminescent spectra (PL) were employed to prove that the coexistence of Ag nanoparticles could boost the photocatalytic efficiency of Ag₂O by decreasing the recombination of photogenerated charge carriers. As shown in Figure 3c, Ag₂O exhibited a strong emission peak in the spectra. In contrast, for Ag/Ag₂O, the peak intensities decreased, suggesting a smaller probability of electron-hole pairs' recombination and reinforced photocatalytic efficiency.³⁶ What is more, ESR spectra obtained from the reaction system after illumination are shown in Figure 3d and e. Upon being irradiated under 808 nm laser (0.5 W/cm²) for 10 min with the attendance of Ag₂O, the characteristic four-line spectrum

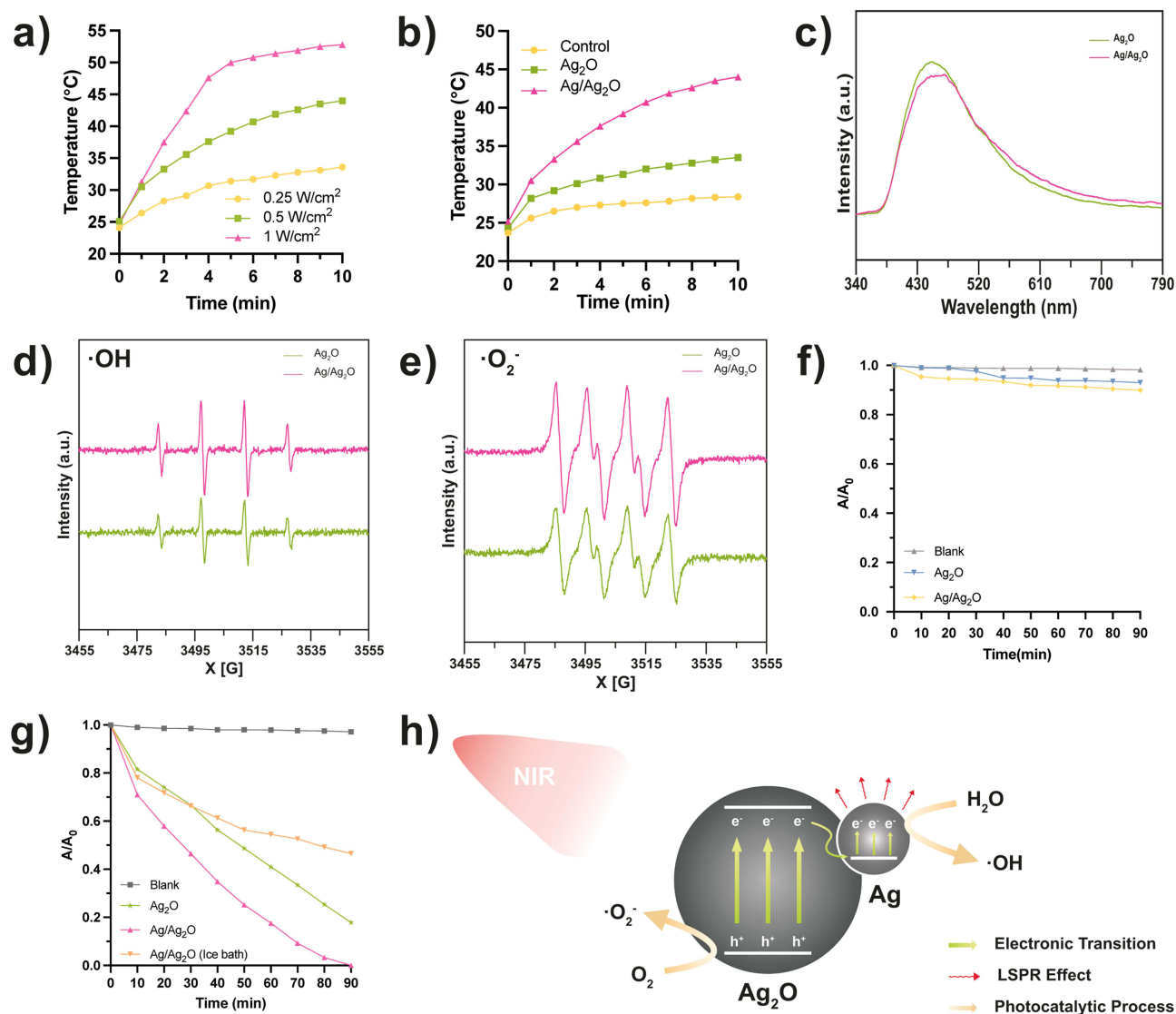


Figure 3 Characterization of photothermal effect and photocatalysis. (a) Temperature-time curves of Ag/Ag₂O (1 mg/mL) under 808 nm NIR laser irradiation of different power intensities. (b) Temperature-time curves of different samples under 808 nm NIR laser irradiation (0.5 W/cm²). (c) Photoluminescence spectra of Ag₂O and Ag/Ag₂O. ESR spectra of $\cdot\text{OH}$ (d) and $\cdot\text{O}_2^-$ (e) were obtained from Ag₂O and Ag/Ag₂O under 808 nm NIR laser irradiation (0.5 W/cm²) for 10 min, respectively. Each group's MB degradation within 90 min without NIR irradiation (f) and with 0.5 W/cm² 808 nm NIR laser irradiation (g). (h) Schematic illustration of the synergistic photocatalysis and photothermal effect for Ag/Ag₂O's photo-responsive process.

of $\cdot\text{OH}$ with relative intensities of 1:2:2:1 appeared. When Ag/Ag₂O hybrids were added, the signal intensity of $\cdot\text{OH}$ increased to about 1.4 times higher than that of Ag₂O. A similar trend was also seen in the spectra of $\cdot\text{O}_2^-$ (Figure 3e), in which the signal intensity of Ag/Ag₂O was about 1.5 times stronger than that of Ag₂O. It therefore could be indicated that both $\cdot\text{OH}$ and $\cdot\text{O}_2^-$ could be generated both in the existence of Ag₂O and Ag/Ag₂O during 808 nm NIR laser irradiation and that deposition of Ag onto Ag₂O enhanced photogeneration of ROS.

Methylene blue (MB) has been prevalently used as an organic dye model to test the photocatalytic efficiency of photocatalysts,^{46–49} so the photocatalytic activities of Ag/Ag₂O were also investigated for MB degradation under such illumination conditions. As shown in Figure 3f, when there was no NIR trigger, the MB solution seldom degraded with any sample within 90 min. Meanwhile, it is demonstrated in Figure 3g that an 808 nm laser at a power intensity of 0.5 W/cm² barely had any influence on the degradation of MB. By contrast, with the attendance of Ag₂O or Ag/Ag₂O, the photo-responsive activities of photocatalysts extensively bolstered the degradation process. Between them, Ag/Ag₂O attained more satisfying results, leading to nearly 100% degradation of MB within 90 min under 0.5 W/cm² NIR

irradiation. In comparison, the degradation rate for the Ag_2O group under the same conditions was 82.1%. The fact that neither Ag_2O nor $\text{Ag}/\text{Ag}_2\text{O}$ could degrade MB in the dark indicated that the declination of MB was primarily assigned to the photo-responsive effects. To further explore the underlying mechanism for $\text{Ag}/\text{Ag}_2\text{O}$ degrading MB, experiments were repeated in the ice bath (Figure 3g), the outcome of which showed that when hindering the local temperature increase, the degradation rate of $\text{Ag}/\text{Ag}_2\text{O}$ after 90 min plummeted from 100% to 82.1%. As for the storage stability (Figure S1A), it was manifested that after usual storage for 15 d, the photocatalytic degradation activity of $\text{Ag}/\text{Ag}_2\text{O}$ (97.5%) did not have a noticeable decrease in comparison with freshly made samples (100%), from which it could be inferred that $\text{Ag}/\text{Ag}_2\text{O}$ was stable at room temperature within 15 days. What is more, there was no significant change in the photocatalytic degradation of MB after 4 experimental cycles for $\text{Ag}/\text{Ag}_2\text{O}$ (Figure S1B), indicating that $\text{Ag}/\text{Ag}_2\text{O}$ had good stability in photo-responsive reactions.

From the studies mentioned above, here came the conclusion that although the temperature at around 45°C alone had no significant impact on the degradation of MB, it could enhance the photocatalytic process of $\text{Ag}/\text{Ag}_2\text{O}$, in which the yield of $\cdot\text{OH}$ as well as $\cdot\text{O}_2^-$ outcompeted Ag_2O . Based on the results above, we supposed that the possible mechanisms for the enhanced photocatalytic performance of $\text{Ag}/\text{Ag}_2\text{O}$ heterostructures lie in the: 1) with the deposition of Ag on the surface of Ag_2O , the formation of heterojunction structures made the separation of photogenerated charge carriers more efficiently, which reduced their recombination, leading to further photocatalytic efficiency acceleration; 2) the temperature rise resulted from the LSPR effect of Ag nanoparticles further enhanced the photocatalytic reaction, possibly by improving the separation of photogenerated charge carriers and the electric field of the surface of Ag.^{50–52} The illustration of the proposed mechanism is shown in Figure 3h.

Antibacterial Assessment

To investigate the antibacterial activities of the samples, *S. aureus* was chosen as the model bacteria. Firstly, from Figure 4a–c, we could tell that a mere NIR laser at a power intensity of $0.5\text{ W}/\text{cm}^2$ barely influenced bacterial viability within 10 min. Nevertheless, when incubated with $1\text{ mg}/\text{mL}$ Ag_2O , the antibacterial rate ascended to 29.7% and 45.8% without or with NIR laser irradiation, respectively. As for $\text{Ag}/\text{Ag}_2\text{O}$ heterostructures, when there was no 808 nm laser irradiation as a trigger, 54.3% of the bacteria was killed, showing a significant increase compared with the Ag_2O group ($P < 0.01$), which indicated that the deposition of AgNPs contributed to the antibacterial activity of $\text{Ag}/\text{Ag}_2\text{O}$. Impressively, once the bacteria suspension was incubated with $\text{Ag}/\text{Ag}_2\text{O}$ under the activation of 808 nm laser ($0.5\text{ W}/\text{cm}^2$), the antibacterial rate increased to 98%, about 2.14 and 1.8 times higher than that of $\text{Ag}_2\text{O}+\text{NIR}$ and $\text{Ag}/\text{Ag}_2\text{O}$ respectively, validating the enhanced antibacterial activities of $\text{Ag}/\text{Ag}_2\text{O}$ under NIR irradiation in comparison with Ag_2O . Additionally, SEM images of *S. aureus* before and after the treatment of $\text{Ag}/\text{Ag}_2\text{O}+\text{NIR}$ are provided in Figure 4d. It was obvious that the bacteria had intact structures before the treatment, while the integrity was destroyed, and the bacteria became wrinkled after the treatment. It has been mentioned in previous studies that the accumulation of local temperature would increase the bacterial membrane permeability, which thus would lead to further damage of ROS to bacteria.⁷ Therefore, it was suggested that during the antibacterial process of $\text{Ag}/\text{Ag}_2\text{O}$ under $0.5\text{ W}/\text{cm}^2$ 808 nm NIR laser irradiation, the local temperature increase, on the one hand, made bacteria more vulnerable; on the other hand, it helped with the ROS production, which then ruined the integrity of bacteria and finally killed them.

The *S. aureus* biofilm model was chosen to verify the biofilm elimination ability of the samples. As CLSM images after LIVE/DEAD staining and the related data analysis results shown in Figure 4e and f, when there was no treatment or with only NIR laser, the biofilm remained nearly intact, with which SEM images after treatment corresponded well (Figure 4g). When there was no trigger of 808 nm laser irradiation, neither Ag_2O nor $\text{Ag}/\text{Ag}_2\text{O}$ showed satisfying antibacterial and biofilm eradication effect, in CLSM images of which the signal intensity of dead bacteria remained at 19.9% (Ag_2O) and 21.5% ($\text{Ag}/\text{Ag}_2\text{O}$), accompanied by the comparatively integral biofilm in SEM images. Once activated by 808 nm laser ($0.5\text{ W}/\text{cm}^2$), the $\text{Ag}_2\text{O}+\text{NIR}$ group realized a boosted antibacterial effect, the antibacterial rate of which climbed to $\sim 30.8\%$. By contrast, the figure of the $\text{Ag}/\text{Ag}_2\text{O}+\text{NIR}$ group raised to $\sim 53.8\%$, showing 2.5 times higher antibacterial efficiency in comparison with sole $\text{Ag}/\text{Ag}_2\text{O}$ ($P < 0.05$). Additionally, we could tell from the SEM images of $\text{Ag}/\text{Ag}_2\text{O}+\text{NIR}$ that most of the biofilm has been eradicated, possibly due to the consequential biofilm degradation after bacterial death, which could also explain that the overall signal intensity in CLSM images was

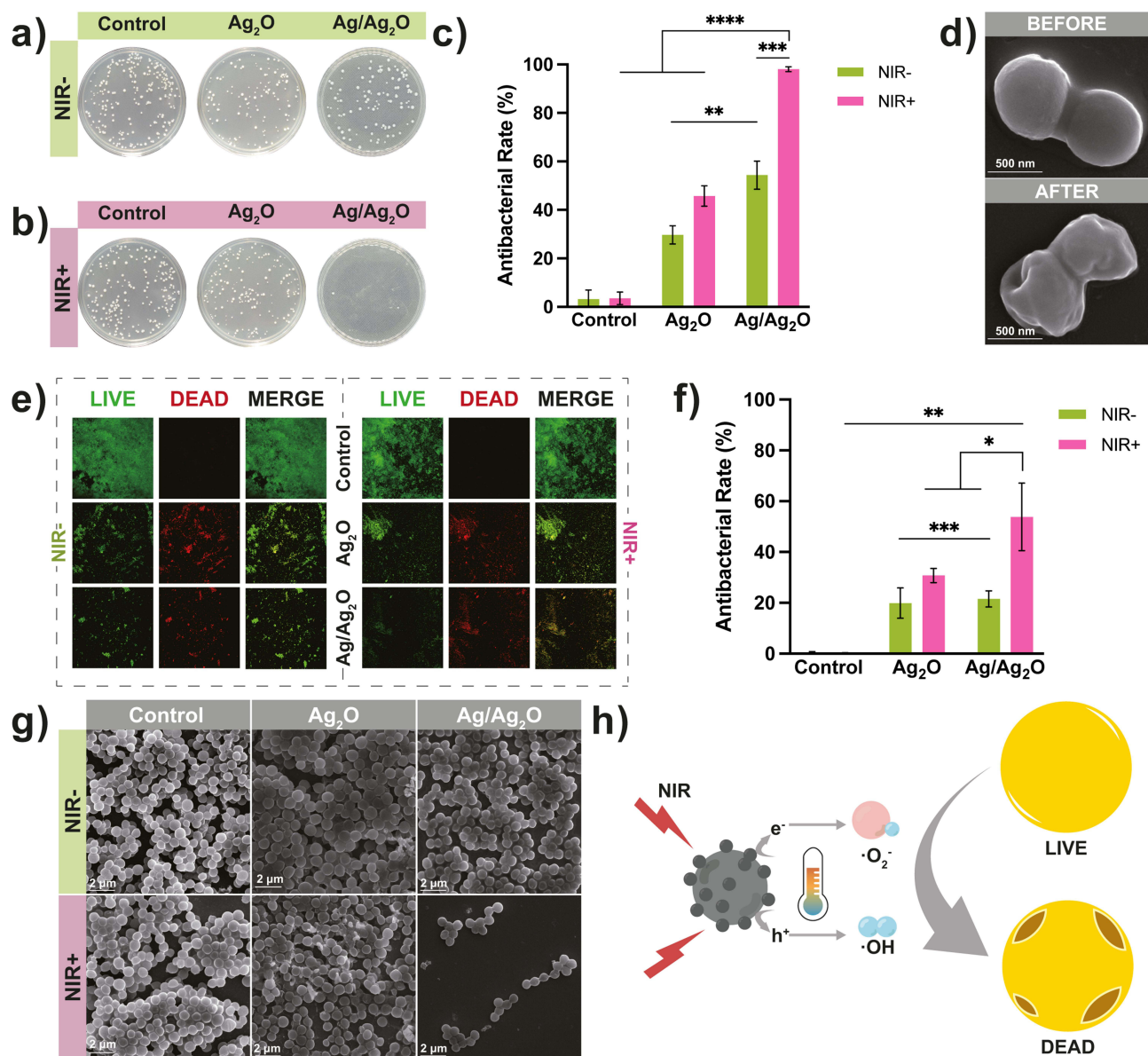


Figure 4 Antibacterial activity against planktonic bacteria and biofilms. Representative photographs of the colony-forming unit of *Staphylococcus aureus* after treatment of each group in the absence (a) and presence (b) of 808 nm NIR laser irradiation (0.5 W/cm^2). (c) Correspondent statistical analysis of each group. (d) Representative SEM images of bacteria before and after being treated with Ag/Ag₂O under 808 nm NIR laser (0.5 W/cm^2) for 10 min. Representative confocal images of Live/Dead assay (e) and correspondent antibacterial rate of bacterial biofilms being treated with each group (f). (g) Representative SEM images of the remained bacterial biofilms after treatment of each group. (h) Schematic illustration of the antibacterial process of Ag/Ag₂O under NIR irradiation (* $P < 0.05$, ** $P < 0.01$, *** $P < 0.001$, **** $P < 0.0001$).

relatively low. Combined with the results above, we believed that Ag/Ag₂O exhibited outstanding antibacterial performance and bacterial biofilm eradication capability when triggered by NIR light, giving credit to the synergistic effect of photocatalysis and LT-PTT, and the proposed scheme is depicted in Figure 4h.

Cytotoxicity and Biocompatibility in vitro

Fibroblast L-929 cells were used to evaluate the biocompatibility and cytotoxicity of Ag/Ag₂O heterostructures in vitro by CCK-8 assay and cell immigration experiments (Figure 5a). The results of CCK-8 assay (Figure 5b) demonstrated that the overall trend of L-929 cells was to proliferate from day 1 to day 3 and decreased from then on to day 5 when incubated with Ag/Ag₂O at low concentrations, but 200 $\mu\text{g/mL}$ of Ag/Ag₂O presented an inhibition effect from the very beginning. Likewise, when the incubated Ag/Ag₂O was at low concentrations, the number of migrated cells was similar to that of the

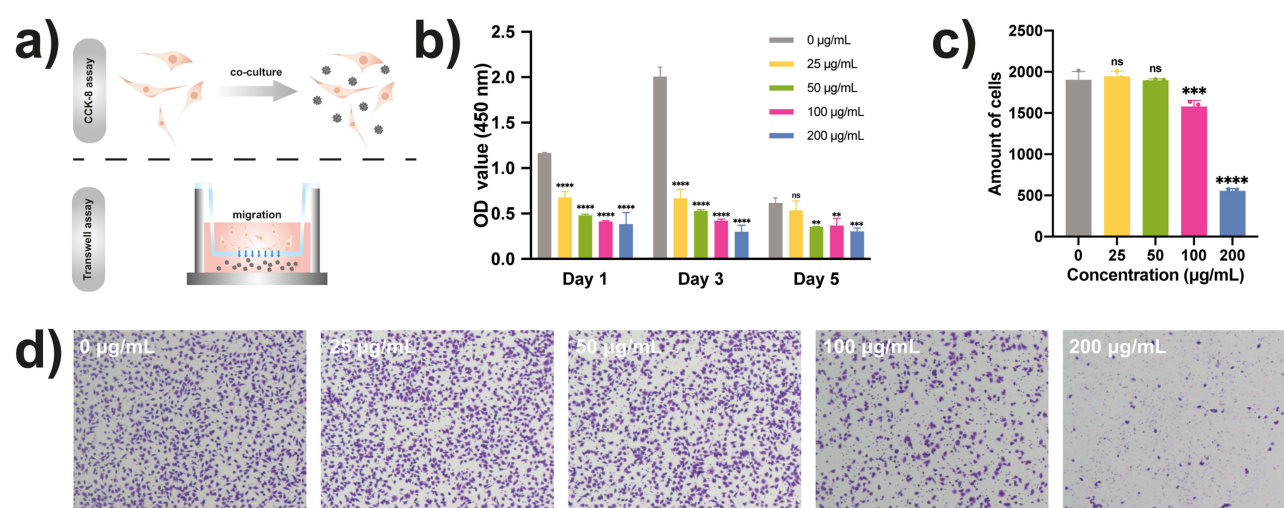


Figure 5 Cytotoxicity and biocompatibility assessment. (a) Schematic illustration of the experiments of evaluating cytocompatibility of Ag/Ag₂O in vitro. (b) CCK-8 assay results after being co-cultured with Ag/Ag₂O at different concentrations (0, 25, 50, 100, 200 µg/mL). The number of migrated cells (c) and representative transwell assay images (d) of Ag/Ag₂O at different concentrations (**P < 0.01, ***P < 0.001, ****P < 0.0001).

control group ($P > 0.05$), while the migration was inhibited at concentrations of 100 and 200 µg/mL (Figure 5c and d). It turned out that the biocompatibility of Ag/Ag₂O was not that ideal. However, it should be noted that the cytotoxicity/biocompatibility are less vital for those externally applied materials, as they were just sprayed or dropped directly onto the lesion areas, other than being introduced to the whole body and major organs via intravenous injection or oral uptakes.⁵³ Besides, the local cytotoxicity generated by water-insoluble solid nanomaterials was quite constricted due to their poor diffusion ability.⁵⁴ Moreover, it has been reported that the cytotoxicity caused by silver nanoparticles was dependent on their intracellular accumulation, from which it could be clued that in our later practical application when the contact time was limited to 10 min, the cytotoxicity of Ag/Ag₂O was acceptable to some extent. Later, histochemical analysis of the wound skin samples of *S. aureus* infection also suggested that Ag/Ag₂O exhibited more promotion during the healing process than local toxicity-induced tissue damage. Together with these results, we could suggest that considering biocompatibility, future exploration of Ag/Ag₂O for biomedical applications could take strategies to diminish its cytotoxicity while sustaining its effective antibacterial performance. To consider future biomedical applications, we may employ biocompatible materials to encapsulate the particles and fabricate a controlled antibacterial platform to lessen its concentration-dependent cytotoxicity. Recent studies have proved it feasible to impregnate AgNPs into a biocompatible hydrogel, not only remaining the strong antibacterial activity of AgNPs but also reducing their cellular toxicity.⁵⁵ Also, the functionalization of nanomaterials has been proven to be useful for the reduced cytotoxicity of nanomaterials without the hindrance of their beneficial effects.⁵⁶ Additionally, both encapsulation and functionalization could endow the nanomaterials with new properties, further broadening the practical application of the materials. Moreover, since silver has been widely applied in the biomedical field, such as antimicrobial agents, drug-delivery carriers, medical device coatings, tissue regeneration, and so on,⁵⁷ we supposed that Ag/Ag₂O could find a way to optimize its biocompatibility for better biomedical application.

In vivo Infected Wound Healing Promotion

S. aureus-infected Sprague-Dawley mice (aged 6–8 w) were employed as model animals to assess the antibacterial efficacy of Ag/Ag₂O heterostructures under 808 nm laser irradiation in vivo. The procedures are illustrated in Figure 6a, and the representative images of the wounds and corresponding statistical analysis are displayed in Figure 6b and c, respectively. From these results, we could tell that the overall wound contraction rate in all four groups rose gradually with time, among which Ag/Ag₂O+NIR exhibited the most effective promotion, achieving a 99.96% decrease in wound area at day 8. The wound area decreased by 70.62% for the Control group and 83.44% for the NIR group (808 nm, 0.5 W/cm²) after 8 days, both of which were significantly less compared with the result of the Ag/Ag₂O+NIR group. As for Ag/Ag₂O group, the decreased wound area was

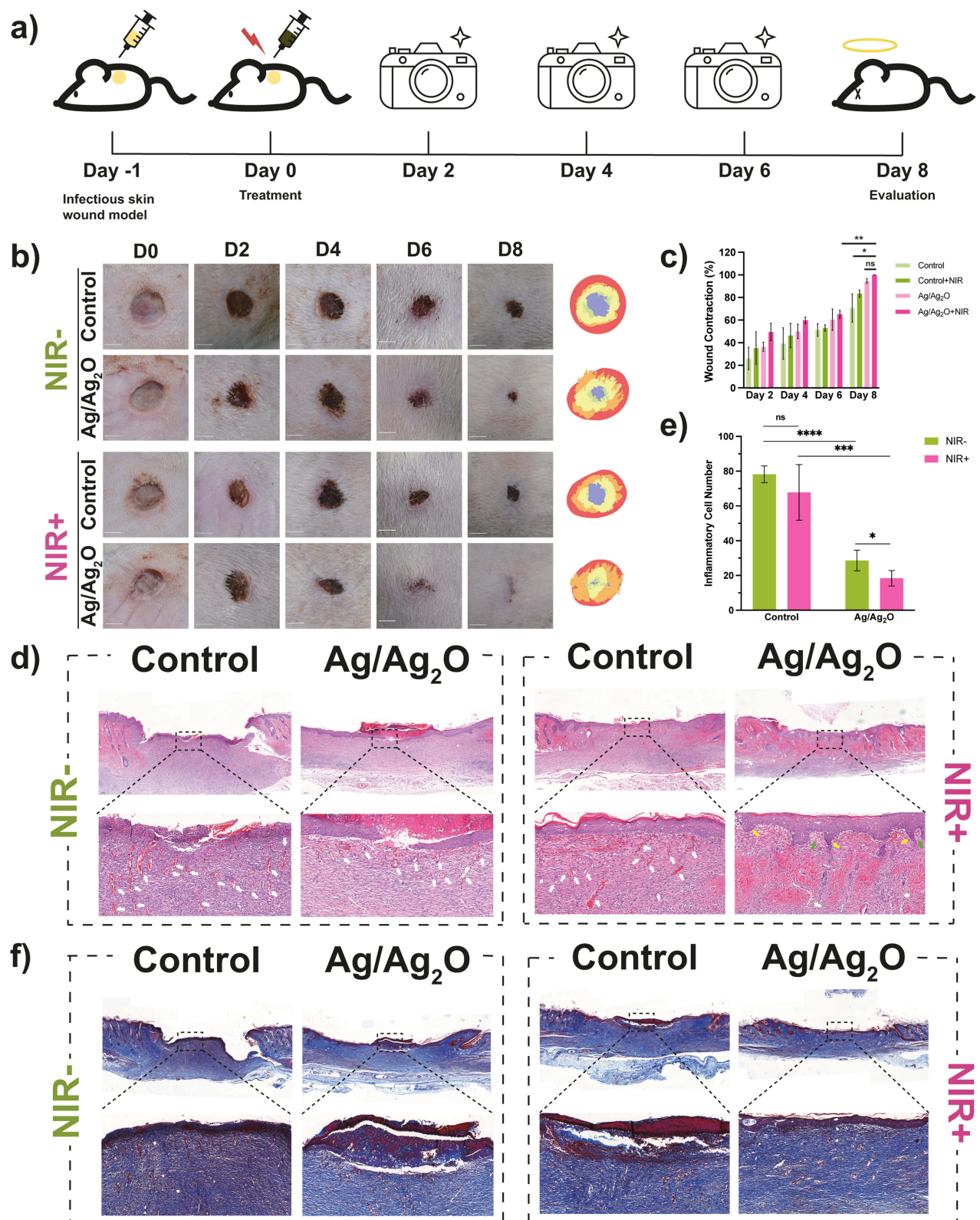


Figure 6 Infectious skin wound healing promotion in vivo. (a) Schematic illustration of the animal model construction and the experimental procedures. (b) Representative photographs of SD mice infectious wounds of each group at different time points. (bar=5 mm) (c) Correspondent calculation of the wound area of each group at different time points. (d) Representative H&E staining images of infectious skin wound samples of each group on Day 8 and correspondent statistical analysis of the inflammation cells (e). (White arrows: neo-vascular formation; yellow arrows: epidermal ridges; green arrows: dermal papillae.) (f) Representative Masson trichrome staining images of infectious skin wound samples of each group on Day 8 (*P < 0.05, **P < 0.01, ***P < 0.001, ****P < 0.0001).

approximately 1.3 times larger than the Control group (~94.57%), although there was no significant difference compared with the Ag/Ag₂O+NIR group. H&E staining (Figure 6d) further demonstrated the change of the skin tissue on the 8th day, from which it was clear that in both the control and NIR group, the hierarchical structures of skin had been damaged, accompanied by severe inflammatory cell immersion and a large quantity of neo-vascular formation (pointed with red arrows). However, from the histochemical level, we could tell the latter group had seen nearly complete re-epithelialization with normal skin tissue hierarchies, which hinted that although the wound contracted to some extent in the Ag/Ag₂O group, the wound healing promotion remained to be unsatisfactory. On the contrary, it could be observed that in Ag/Ag₂O+NIR group, the whole skin tissue realized orderly healing of full skin layers, including the formation of epidermal ridges and dermal papillae (pointed with white arrows and green arrows), symbols of the tighter connection between the epidermal layer and the dermal layer. Specifically, the inflammatory cells in the H&E-stained slides were statistically analyzed. From the results (Figure 6e), it was shown that when there was no light irradiation, the Ag/Ag₂O group exhibited boosted wound healing promotion and a lower level of inflammation compared with the Control group ($P < 0.0001$). When given NIR irradiation (808 nm, 0.5 W/cm²) for 10 min, there was still no significant change in the inflammation level of the Control+NIR group compared with the Control group. As for the Ag/Ag₂O+NIR group, when given the same light irradiation, the inflammation cells decreased by ~35.7% in comparison with the Ag/Ag₂O group ($P < 0.05$) and ~72.9% in comparison with the Control+NIR group ($P < 0.001$), showing the enhanced inflammation amelioration of this group. The representative Masson trichrome staining images (Figure 6f) also exhibited a similar trend, in which the skin tissues of the Ag/Ag₂O+NIR group showed abundant collagen fiber deposition. These results were in good accordance with previous antibacterial assessments *in vitro* and infectious wound contraction *in vivo*, which further verified the improved antibacterial activity of Ag/Ag₂O under 0.5 W/cm² 808 nm NIR irradiation and the consequent infectious wound healing promotion. Therefore, it could be concluded that among all groups, the Ag/Ag₂O+NIR group saw the most wound contraction within 8 days and acquired nearly complete wound healing from a histochemical level.

Conclusion

Overall, Ag/Ag₂O was fabricated through a facile two-step method without special facilities and harsh conditions. With photo-responsibility under 808 nm NIR laser irradiation, Ag/Ag₂O then acted as an effective bactericidal agent with the synergistic effect of LT-PTT and photocatalysis. The mild local temperature increase boosted the photocatalytic performance of Ag/Ag₂O and the resultant ROS generation. The results of *in vitro* experiments indicated that the excellent NIR-triggered ROS production and temperature accumulation of Ag/Ag₂O improved the antibacterial efficiency, which outperformed Ag₂O, an intrinsic narrow band gap semiconductor. In addition, although Ag/Ag₂O exhibited cytotoxicity at higher concentrations *in vitro*, it effectively enhanced the wound contraction in an infectious skin wound model, the tissue of which group exhibited approximately complete re-epithelialization from the histochemical level. Consequently, it was proved that Ag/Ag₂O could act as a promising bactericidal agent for infectious wound treatment and skin regeneration.

Abbreviations

NIR, near-infrared; ROS, reactive oxygen species; LSPR, local surface plasmon resonance; MB, methylene blue; LT-PTT, low-temperature photothermal therapy.

Acknowledgments

This study was supported by the National Natural Science Foundation of China (grant number 81970968, 32271415), the National Key R&D Program of China (grant number 2022YFA1100036), the Sichuan Science and Technology Program (grant number 2022YFS0283).

Disclosure

The authors report no conflicts of interest in this work.

References

- Li S, Dong S, Xu W, et al. Antibacterial hydrogels. *Adv Sci*. 2018;5(5):1700527. doi:10.1002/advs.201700527
- Ma J, Jiang L, Liu G. Cell membrane-coated nanoparticles for the treatment of bacterial infection. *Wiley Interdiscip Rev*. 2022;14(5):e1825. doi:10.1002/wnan.1825
- Lungu IA, Moldovan OL, Biriş V, Rusu A. Fluoroquinolones hybrid molecules as promising antibacterial agents in the fight against antibacterial resistance. *Pharmaceutics*. 2022;14(8):1749. doi:10.3390/pharmaceutics14081749
- Cao Z, Luo Y, Li Z, et al. Antibacterial hybrid hydrogels. *Macromol Biosci*. 2021;21(1):2000252. doi:10.1002/mabi.202000252
- Bi X, Bai Q, Liang M, et al. Silver peroxide nanoparticles for combined antibacterial sonodynamic and photothermal therapy. *Small*. 2022;18(2):2104160. doi:10.1002/sml.202104160
- Hasan M, Zafar A, Shahzadi I, et al. Fractionation of biomolecules in withania coagulans extract for bio-reductive nanoparticle synthesis, antifungal and biofilm activity. *Molecules*. 2020;25(15):3478. doi:10.3390/molecules25153478
- Ren Y, Liu H, Liu X, et al. Photoresponsive materials for antibacterial applications. *Cell Rep Phys Sci*. 2020;1(11):100245. doi:10.1016/j.xcrp.2020.100245
- Naskar A, Kim K. Photo-stimuli-responsive nanomaterials as cutting-edge platform materials for antibacterial applications. *Pharmaceutics*. 2022;14(11):2343. doi:10.3390/pharmaceutics14112343
- Liu Z, Jiang X, Li Z, et al. Recent progress of photo-excited antibacterial materials via chemical vapor deposition. *Chem Eng J*. 2022;437:135401. doi:10.1016/j.cej.2022.135401
- Han Q, Lau JW, Do TC, Zhang Z, Xing B. Near-infrared light brightens bacterial disinfection: recent progress and perspectives. *ACS Appl Bio Mater*. 2021;4(5):3937–3961. doi:10.1021/acsabm.0c01341
- Zhao J, Zhong D, Zhou S. NIR-I-to-NIR-II fluorescent nanomaterials for biomedical imaging and cancer therapy. *J Mater Chem B*. 2018;6(3):349–365. doi:10.1039/C7TB02573D
- Gupta R, Modak JM, Madras G. Behavioral analysis of simultaneous photo-electro-catalytic degradation of antibiotic resistant E. coli and antibiotic via ZnO/CuI: a kinetic and mechanistic study. *Nanoscale Adv*. 2019;1(10):3992–4008. doi:10.1039/c9na00483a
- Yang R, Song G, Wang L, et al. Full solar-spectrum-driven antibacterial therapy over hierarchical Sn3O4/PDINH with enhanced photocatalytic activity. *Small*. 2021;17(39):2102744. doi:10.1002/sml.202102744
- Li S, Huo H, Gao X, et al. Engineering Janus gold nanorod-titania heterostructures with enhanced photocatalytic antibacterial activity against multidrug-resistant bacterial infection. *Nano Res*. 2018;1:34. doi:10.1007/s12274-022-4876-5
- Saif MS, Zafar A, Waqas M, et al. Phyto-reflexive zinc oxide nano-flowers synthesis: an advanced photocatalytic degradation and infectious therapy. *J Mater Res Technol*. 2021;13:2375–2391. doi:10.1016/j.jmrt.2021.05.107
- Wang G, Ma X, Huang B, et al. Controlled synthesis of Ag2O microcrystals with facet-dependent photocatalytic activities. *J Mater Chem*. 2012;22(39):21189–21194. doi:10.1039/C2JM35010F
- Jiang W, Wang X, Wu Z, et al. Silver oxide as superb and stable photocatalyst under visible and near-infrared light irradiation and its photocatalytic mechanism. *Ind Eng Chem Res*. 2015;54(3):832–841. doi:10.1021/ie503241k
- Lu W, Shu J, Wang Z, Huang N, Song W. The intrinsic oxidase-like activity of Ag2O nanoparticles and its application for colorimetric detection of sulfite. *Mater Lett*. 2015;154:33–36. doi:10.1016/j.matlet.2015.04.051
- Qin J, Dou Y, Wu F, et al. In-situ formation of Ag2O in metal-organic framework for light-driven upcycling of microplastics coupled with hydrogen production. *Appl Catal B Environ*. 2022;319:121940. doi:10.1016/j.apcatb.2022.121940
- Wen XJ, Niu CG, Zhang L, Liang C, Zeng GM. A novel Ag2O/CeO2 heterojunction photocatalysts for photocatalytic degradation of enrofloxacin: possible degradation pathways, mineralization activity and an in depth mechanism insight. *Appl Catal B Environ*. 2018;221:701–714. doi:10.1016/j.apcatb.2017.09.060
- Jiang W, Fu H, Zhu Y, Yue H, Yuan S, Liang B. Floatable superhydrophobic Ag2O photocatalyst without a modifier and its controllable wettability by particle size adjustment. *Nanoscale*. 2018;10(28):13661–13672. doi:10.1039/C8NR02581A
- Dharmaraj D, Krishnamoorthy M, Rajendran K, et al. Antibacterial and cytotoxicity activities of biosynthesized silver oxide (Ag2O) nanoparticles using Bacillus paramycoides. *J Drug Deliv Sci Technol*. 2021;61:102111. doi:10.1016/j.jddst.2020.102111
- Li D, Chen S, Zhang K, et al. The interaction of Ag2O nanoparticles with Escherichia coli: inhibition–sterilization process. *Sci Rep*. 2021;11(1):1703. doi:10.1038/s41598-021-81305-5
- Wang X, Wu HF, Kuang Q, Huang RB, Xie ZX, Zheng LS. Shape-dependent antibacterial activities of Ag2O polyhedral particles. *Langmuir*. 2010;26(4):2774–2778. doi:10.1021/la9028172
- Hu X, Hu C, Wang R. Enhanced solar photodegradation of toxic pollutants by long-lived electrons in Ag–Ag2O nanocomposites. *Appl Catal B Environ*. 2015;176–177:637–645. doi:10.1016/j.apcatb.2015.04.040
- Li M, Wang Y, Xing Y, Zhong J. P123-assisted preparation of Ag/Ag2O with significantly enhanced photocatalytic performance. *Solid State Sci*. 2020;99:106062. doi:10.1016/j.solidstatesciences.2019.106062
- Zhou Z, Li B, Liu X, et al. Recent progress in photocatalytic antibacterial. *ACS Appl Bio Mater*. 2021;4(5):3909–3936. doi:10.1021/acsabm.0c01335
- Li G, Yang C, He Q, Liu J. Ag-based photocatalytic heterostructures: construction and photocatalytic energy conversion application. *J Environ Chem Eng*. 2022;10(3):107374. doi:10.1016/j.jece.2022.107374
- Chang M, Wang M, Chen Y, et al. Self-assembled CeVO4/Ag nanohybrid as photoconversion agents with enhanced solar-driven photocatalysis and NIR-responsive photothermal/photodynamic synergistic therapy performance. *Nanoscale*. 2019;11(20):10129–10136. doi:10.1039/C9NR02412C
- D'Agostino A, Taglietti A, Desando R, et al. Bulk surfaces coated with triangular silver nanoplates: antibacterial action based on silver release and photo-thermal effect. *Nanomaterials*. 2017;7(1):7. doi:10.3390/nano7010007
- Mehrabani MG, Karimian R, Mehrmouz B, Rahimi M, Kafili HS. Preparation of biocompatible and biodegradable silk fibroin/chitin/silver nanoparticles 3D scaffolds as a bandage for antimicrobial wound dressing. *Int J Biol Macromol*. 2018;114:961–971. doi:10.1016/j.ijbiomac.2018.03.128
- Tang S, Zheng J. Antibacterial activity of silver nanoparticles: structural effects. *Adv Health Mater*. 2018;7(13):1701503. doi:10.1002/adhm.201701503

33. Yin IX, Zhang J, Zhao IS, Mei ML, Li Q, Chu CH. The antibacterial mechanism of silver nanoparticles and its application in dentistry. *Int J Nanomedicine*. 2020;15:2555–2562. doi:10.2147/IJN.S246764
34. Dong X, Ji X, Jing J, Li M, Li J, Yang W. Synthesis of triangular silver nanoprisms by stepwise reduction of sodium borohydride and trisodium citrate. *J Phys Chem C*. 2010;114(5):2070–2074. doi:10.1021/jp909964k
35. Xu Q, Chang M, Zhang Y, et al. PDA/Cu bioactive hydrogel with “Hot Ions Effect” for inhibition of drug-resistant bacteria and enhancement of infectious skin wound healing. *ACS Appl Mater Interfaces*. 2020;12(28):31255–31269. doi:10.1021/acsami.0c08890
36. Xu H, Xie J, Jia W, Wu G, Cao Y. The formation of visible light-driven Ag/Ag₂O photocatalyst with excellent property of photocatalytic activity and photocorrosion inhibition. *J Colloid Interface Sci*. 2018;516:511–521. doi:10.1016/j.jcis.2018.01.071
37. Yang H, Tian J, Li T, Cui H. Synthesis of novel Ag/Ag₂O heterostructures with solar full spectrum (UV, visible and near-infrared) light-driven photocatalytic activity and enhanced photoelectrochemical performance. *Catal Commun*. 2016;87:82–85. doi:10.1016/j.catcom.2016.09.013
38. Huang L, Chen R, Luo J, Hasan M, Shu X. Synthesis of phytogenic silver nanoparticles as bacterial and ATP energy silencer. *J Inorg Biochem*. 2022;231:111802. doi:10.1016/j.jinorgbio.2022.111802
39. Zulfiqar H, Zafar A, Rasheed MN, et al. Synthesis of silver nanoparticles using *Fagonia cretica* and their antimicrobial activities. *Nanoscale Adv*. 2019;1(5):1707–1713. doi:10.1039/C8NA00343B
40. Haq S, Rehman W, Waseem M, et al. Fabrication of pure and moxifloxacin functionalized silver oxide nanoparticles for photocatalytic and antimicrobial activity. *J Photochem Photobiol B*. 2018;186:116–124. doi:10.1016/j.jphotobiol.2018.07.011
41. Vinay SP, Udayabhanu NG, Chandrappa CP, Chandrasekhar N. Novel Gomutra (cow urine) mediated synthesis of silver oxide nanoparticles and their enhanced photocatalytic, photoluminescence and antibacterial studies. *J Sci Adv Mater Devices*. 2019;4(3):392–399. doi:10.1016/j.jsamd.2019.08.004
42. Kim D, Kim H. Induction of apoptotic temperature in photothermal therapy under various heating conditions in multi-layered skin structure. *Int J Mol Sci*. 2021;22(20):11091. doi:10.3390/ijms222011091
43. Li K, Ma X, He S, et al. Ultrathin nanosheet-supported Ag@Ag₂O core-shell nanoparticles with vastly enhanced photothermal conversion efficiency for NIR-II-triggered photothermal therapy. *ACS Biomater Sci Eng*. 2022;8(2):540–550. doi:10.1021/acsbiomaterials.1c01291
44. Verma P, Yuan K, Kuwahara Y, Mori K, Yamashita H. Enhancement of plasmonic activity by Pt/Ag bimetallic nanocatalyst supported on mesoporous silica in the hydrogen production from hydrogen storage material. *Appl Catal B Environ*. 2018;223:10–15. doi:10.1016/j.apcatb.2017.05.017
45. Waiskopf N, Ben-Shahar Y, Banin U. Photocatalytic hybrid semiconductor-metal nanoparticles; from synergistic properties to emerging applications. *Adv Mater*. 2018;30(41):1706697. doi:10.1002/adma.201706697
46. Abou-Gamra ZM, Ahmed MA. Synthesis of mesoporous TiO₂-curcumin nanoparticles for photocatalytic degradation of methylene blue dye. *J Photochem Photobiol B*. 2016;160:134–141. doi:10.1016/j.jphotobiol.2016.03.054
47. Houas A, Lachheb H, Ksibi M, Elaloui E, Guillard C, Herrmann JM. Photocatalytic degradation pathway of methylene blue in water. *Appl Catal B Environ*. 2001;31(2):145–157. doi:10.1016/S0926-3373(00)00276-9
48. Kuo WS, Ho PH. Solar photocatalytic decolorization of methylene blue in water. *Chemosphere*. 2001;45(1):77–83. doi:10.1016/S0045-6535(01)00008-X
49. Sirajudheen P, Meenakshi S. Facile synthesis of chitosan-La³⁺-graphite composite and its influence in photocatalytic degradation of methylene blue. *Int J Biol Macromol*. 2019;133:253–261. doi:10.1016/j.ijbiomac.2019.04.073
50. Barakat NAM, Kanjwal MA, Chronakis IS, Kim HY. Influence of temperature on the photodegradation process using Ag-doped TiO₂ nanostructures: negative impact with the nanofibers. *J Mol Catal Chem*. 2013;366:333–340. doi:10.1016/j.molcata.2012.10.012
51. Chen YW, Hsu YH. Effects of reaction temperature on the photocatalytic activity of TiO₂ with Pd and Cu cocatalysts. *Catalysts*. 2021;11(8):966. doi:10.3390/catal11080966
52. Kumar A. A review on the factors affecting the photocatalytic degradation of hazardous materials. *Mater Sci Eng Int J*. 2017;1. doi:10.15406/mseij.2017.01.00018
53. Thangudu S, Kulkarni SS, Vankayala R, Chiang CS, Hwang KC. Photosensitized reactive chlorine species-mediated therapeutic destruction of drug-resistant bacteria using plasmonic core-shell Ag@AgCl nanocubes as an external nanomedicine. *Nanoscale*. 2020;12(24):12970–12984. doi:10.1039/D0NR01300E
54. Brunner TJ, Wick P, Manser P, et al. In vitro cytotoxicity of oxide nanoparticles: comparison to asbestos, silica, and the effect of particle solubility. *Environ Sci Technol*. 2006;40(14):4374–4381. doi:10.1021/es052069i
55. Haidari H, Kopecki Z, Bright R, et al. Ultrasmall AgNP-impregnated biocompatible hydrogel with highly effective biofilm elimination properties. *ACS Appl Mater Interfaces*. 2020;12(37):41011–41025. doi:10.1021/acsami.0c09414
56. Wijesundera SA, Jayawardana KW, Yan M. Trehalose-modified silver nanoparticles as antibacterial agents with reduced cytotoxicity and enhanced uptake by mycobacteria. *ACS Appl Nano Mater*. 2022;5(8):10704–10714. doi:10.1021/acsanm.2c02047
57. Burduşel AC, Gherasim O, Grumezescu AM, Mogoantă L, Fica A, Andronescu E. Biomedical applications of silver nanoparticles: an up-to-date overview. *Nanomaterials*. 2018;8(9):681. doi:10.3390/nano8090681